

ASYMMETRIC MAGNETIC RECONNECTION IN SOLAR FLARE AND CORONAL MASS EJECTION CURRENT SHEETS

N. A. MURPHY¹, M. P. MIRALLES¹, C. L. POPE^{1,2}, J. C. RAYMOND¹, H. D. WINTER¹, K. K. REEVES¹,
D. B. SEATON³, A. A. VAN BALLEGOOIJEN¹, AND J. LIN^{1,4}

¹ Harvard-Smithsonian Center for Astrophysics, 60 Garden Street, Cambridge, MA 02138, USA

² Elmhurst College, Elmhurst, IL, USA

³ SIDC-Royal Observatory of Belgium, Avenue Circulaire 3, 1180 Brussels, Belgium

⁴ Yunnan Astronomical Observatory, Chinese Academy of Sciences, P.O. Box 110, Kunming, Yunnan 650011, China

Received 2012 January 25; accepted 2012 March 17; published 2012 May 4

ABSTRACT

We present two-dimensional resistive magnetohydrodynamic simulations of line-tied asymmetric magnetic reconnection in the context of solar flare and coronal mass ejection current sheets. The reconnection process is made asymmetric along the inflow direction by allowing the initial upstream magnetic field strengths and densities to differ, and along the outflow direction by placing the initial perturbation near a conducting wall boundary that represents the photosphere. When the upstream magnetic fields are asymmetric, the post-flare loop structure is distorted into a characteristic skewed candle flame shape. The simulations can thus be used to provide constraints on the reconnection asymmetry in post-flare loops. More hard X-ray emission is expected to occur at the footpoint on the weak magnetic field side because energetic particles are more likely to escape the magnetic mirror there than at the strong magnetic field footpoint. The footpoint on the weak magnetic field side is predicted to move more quickly because of the requirement in two dimensions that equal amounts of flux must be reconnected from each upstream region. The X-line drifts away from the conducting wall in all simulations with asymmetric outflow and into the strong magnetic field region during most of the simulations with asymmetric inflow. There is net plasma flow across the X-line for both the inflow and outflow directions. The reconnection exhaust directed away from the obstructing wall is significantly faster than the exhaust directed toward it. The asymmetric inflow condition allows net vorticity in the rising outflow plasmoid which would appear as rolling motions about the flux rope axis.

Key words: magnetic reconnection – methods: numerical – Sun: coronal mass ejections (CMEs) – Sun: flares

Online-only material: color figures

1. INTRODUCTION

Flux rope models of coronal mass ejections (CMEs) predict the formation of an elongated current sheet in the wake behind the rising plasmoid (e.g., Sturrock 1966; Hirayama 1974; Kopp & Pneuman 1976; Lin & Forbes 2000). Reconnection in these current sheets increases the flux contained within the rising plasmoid and reduces the amount of flux confining the plasmoid to low heights. Lin et al. (2004) predict that these current sheets contribute substantially to the mass budgets of CMEs, such that the final parameters for CME evolution for interplanetary propagation are not set until the flux rope reaches several solar radii. CME current sheets may also play an important role in the CME energy budget (Rakowski et al. 2007; Reeves et al. 2010; Murphy 2010; Murphy et al. 2011).

In recent years, several features identified as current sheets have been observed during and after CMEs (Ciaravella et al. 2002; Ko et al. 2003; Sui & Holman 2003; Webb et al. 2003; Lin et al. 2005, 2009; Bemporad et al. 2006; Ciaravella & Raymond 2008; Bemporad 2008; Vršnak et al. 2009; Saint-Hilaire et al. 2009; Schettino et al. 2010; Liu et al. 2010; Savage et al. 2010, 2011; Patsourakos & Vourlidas 2011; Reeves & Golub 2011; Landi et al. 2012). These features usually appear as long-lasting bright streaks when viewed edge-on in white-light observations by the Large Angle and Spectrometric Coronagraph (LASCO; Brueckner et al. 1995) on the *Solar and Heliospheric Observatory (SOHO)*. Several events observed by LASCO were also observed by the Ultraviolet Coronagraph Spectrometer (UVCS; Kohl et al. 1995) on *SOHO* in [Fe XVIII] and Si XII. LASCO images occasionally show large blobs (e.g.,

Lin et al. 2005) that are possibly the result of merging plasmoids (Fermo et al. 2010; Uzdensky et al. 2010; Loureiro et al. 2011), although the UVCS detection of strong C III emission in a few of these features has indicated that this low ionization state plasma was not processed through the current sheet. While these blobs have been interpreted as propagating at or near the Alfvén velocity, V_A , simulations show that large magnetic islands often propagate at a velocity ~ 2 – 4 times slower (e.g., Shen et al. 2011). Frequently, these current sheet features are observed to drift or tilt with time, including during the “Cartwheel CME” (Savage et al. 2010; Landi et al. 2010, 2012) observed by the X-Ray Telescope (XRT) on *Hinode* on 2008 April 9. The magnetic field topology and field strengths in and around CME current sheets are not well understood because of the lack of appropriate diagnostics.

Magnetic reconnection with asymmetry in the inflow direction occurs in Earth’s dayside magnetopause (Phan & Paschmann 1996; Ku & Sibeck 1997), Earth’s magnetotail (Øieroset et al. 2004), laboratory plasma experiments (Yamada et al. 1997; Murphy & Sovinec 2008), plasma turbulence (Servidio et al. 2009, 2010), and during the merging of unequal flux ropes (Linton 2006). The scaling of asymmetric inflow reconnection has been investigated by Cassak & Shay (2007, 2008, 2009), who find that the reconnection rate depends on a hybrid Alfvén speed that is a function of the density and magnetic field strength in both upstream regions, given in dimensionless form by

$$V_{Ah}^2 = \frac{B_L B_R (B_L + B_R)}{\rho_L B_R + \rho_R B_L}, \quad (1)$$

where B_L and B_R are the upstream magnetic field strengths and ρ_L and ρ_R are the upstream densities (see also Borovsky & Hesse 2007; Birn et al. 2008, 2010). Simulations persistently show that the flow stagnation point and magnetic field null are separated by a short distance, and that the X-line usually drifts toward the region with the stronger magnetic field (Ugai 2000; Cassak & Shay 2007; Murphy & Sovinec 2008). The current sheet drifting is less prevalent when a spatially localized resistivity is imposed (e.g., Borovsky & Hesse 2007; Birn et al. 2008). When there is a pressure gradient along the inflow direction during guide field reconnection, the X-line diamagnetically drifts along the outflow direction. Reconnection is suppressed when the drift velocity is comparable to the Alfvén velocity (Rogers & Zakharov 1995; Swisdak et al. 2003; Phan et al. 2010; Beidler & Cassak 2011).

CME current sheets form in a stratified atmosphere and thus are expected to be asymmetric along the outflow direction as well. Asymmetric outflow reconnection occurs in the solar atmosphere (Kopp & Pneuman 1976; Lin & Forbes 2000; Ciaravella & Raymond 2008), planetary magnetotails (Oka et al. 2011), and laboratory plasma experiments (Ono et al. 1993, 1997; Inomoto et al. 2006; Lin et al. 2008; Murphy & Sovinec 2008; Gray et al. 2010). Murphy et al. (2010) derived scaling relations for a long and thin current sheet with asymmetric downstream pressure and found that the reconnection rate is not greatly affected unless outflow is blocked from both ends of the current sheet. Simulations of asymmetric outflow reconnection and X-line retreat show that the X-line and flow stagnation point are separated by a short distance and that most of the energy released during reconnection is directed toward the unobstructed current sheet exit (Roussev et al. 2001; Galsgaard & Roussev 2002; Oka et al. 2008; Reeves et al. 2010; Murphy 2010; Shen et al. 2011). Asymmetry and motion of magnetic nulls have recently been considered in three-dimensional configurations (e.g., Al-Hachami & Pontin 2010; Galsgaard & Pontin 2011; Gray et al. 2010; Lukin & Linton 2011).

In this work, we simulate magnetic reconnection that is asymmetric in both the inflow and outflow directions and consider the effects that these asymmetries may have on solar flare and CME current sheets. In Section 2, we discuss the numerical method used by the NIMROD code and the simulation setup. In Section 3, we present the simulation results, including the magnetic structure, flow pattern, X-line dynamics, vorticity in the outflow plasmoid, and the morphology of the post-flare loops. In Section 4, we derive an analytic solution for the potential field structure of asymmetric post-flare loops and discuss the connection with the simulation results. In Section 5, we discuss expected observational signatures of line-tied asymmetric reconnection during solar eruptions. Section 6 contains a summary and a discussion of our results.

2. NUMERICAL METHOD AND SIMULATION SETUP

The NIMROD code (Sovinec et al. 2004, 2005, 2010) solves the equations of extended magnetohydrodynamics (MHD) using a finite element formulation for the poloidal plane, and for three-dimensional simulations, a finite Fourier series expansion for the out-of-plane direction. In dimensionless form, the equations solved for the two-dimensional simulations reported in this paper are

$$\frac{\partial \rho}{\partial t} + \nabla \cdot (\rho \mathbf{V}) = \nabla \cdot D \nabla \rho, \quad (2)$$

$$\frac{\partial \mathbf{B}}{\partial t} = -\nabla \times (\eta \mathbf{J} - \mathbf{V} \times \mathbf{B}), \quad (3)$$

$$\mathbf{J} = \nabla \times \mathbf{B}, \quad (4)$$

$$\rho \left(\frac{\partial \mathbf{V}}{\partial t} + \mathbf{V} \cdot \nabla \mathbf{V} \right) = \mathbf{J} \times \mathbf{B} - \nabla p + \nabla \cdot \rho \nu \nabla \mathbf{V}, \quad (5)$$

$$\frac{\rho}{\gamma - 1} \left(\frac{\partial T}{\partial t} + \mathbf{V} \cdot \nabla T \right) = -\frac{p}{2} \nabla \cdot \mathbf{V} - \nabla \cdot \mathbf{q} + Q, \quad (6)$$

where \mathbf{B} is the magnetic field, \mathbf{J} is the current density, \mathbf{V} is the bulk plasma velocity, p is the plasma pressure, ρ is the density, η is the resistivity, ν is the kinematic viscosity, D is an artificial number density diffusivity, T is the temperature, $\gamma = 5/3$ is the ratio of specific heats, and Q includes Ohmic and viscous heating. The heat flux vector includes the effects of anisotropic thermal conduction and is given by $\mathbf{q} = -\rho[\chi_{\parallel} \hat{\mathbf{b}}\hat{\mathbf{b}} + \chi_{\perp}(\mathbf{I} - \hat{\mathbf{b}}\hat{\mathbf{b}})] \cdot \nabla T$, where $\hat{\mathbf{b}}$ is a unit vector in the direction of the magnetic field. The normalizations are given by B_0 , ρ_0 , L_0 , t_0 , $V_{A0} \equiv B_0/\sqrt{\mu_0 \rho} \equiv L_0/t_0$, $p_0 \equiv B_0/\mu_0 \equiv \rho_0 V_{A0}^2$, $J_0 \equiv B_0/\mu_0 L_0$, and $\eta_0/\mu_0 \equiv \nu_0 \equiv \chi_0 \equiv D_0 \equiv L_0^2/t_0$. Divergence cleaning is used to prevent the buildup of divergence error (Sovinec et al. 2004). A small number density diffusivity ($D \ll \eta$) is included to ensure that the number density profile remains sufficiently smooth in regions of sharp gradients. Except as noted, all velocities are in the simulation reference frame. Additional details for the numerical method, normalizations, and simulation setup are presented by Murphy (2010).

Rather than modeling a solar eruption in detail, we choose an idealized initial condition that allows asymmetric reconnection to commence. The initial conditions are of a perturbed, modified Harris sheet that allows asymmetric upstream magnetic field strengths, densities, and plasma pressure (see Birn et al. 2008, 2010). We define $\hat{\mathbf{x}}$ as the inflow direction, $\hat{\mathbf{y}}$ as the outflow direction, and $\hat{\mathbf{z}}$ as the out-of-plane direction. The initial equilibrium is given by

$$\mathbf{B}(x) = B_{R0} \left[\frac{\tanh\left(\frac{x}{\delta_0} - b\right) + b}{1 + b} \right] \hat{\mathbf{y}} + B_{z0} \hat{\mathbf{z}} \quad (7)$$

$$p(x) = \frac{1}{2} (1 - B_y^2) + \beta_{R0} \frac{B_{R0}^2}{2} \quad (8)$$

$$\rho(x) = \rho_0 [1 + (f_0 - 1)(1 - \lambda^2)], \quad (9)$$

$$\lambda \equiv \frac{1}{2} \left[1 + \tanh\left(\frac{x}{\delta_0} - b\right) \right], \quad (10)$$

where δ_0 is the initial current sheet thickness, b is the magnetic asymmetry parameter, B_{z0} is the initial guide field (equal to zero except in case F where $B_{z0} = 4$), and $\beta_{R0} = p_{R0}/(B_{R0}^2/2)$. Note that β_{R0} does not include the guide field contribution. The subscripts “L” and “R” refer to the asymptotic magnitudes of quantities for $x < 0$ and $x > 0$, respectively, and the subscript “0” refers to the values of quantities at the beginning of each simulation. The initial ratios for the upstream densities and magnetic fields are given by

$$f_0 \equiv \frac{\rho_{L0}}{\rho_{R0}}, \quad (11)$$

Table 1
Simulation Parameters

Case	m_x	m_y	V_{Ah0}	R_0	f_0	B_{z0}	S_h^a	Notes
A	24	80	1.00	1.0	1	0	8000	Symmetric inflow
B	60	80	0.71	0.5	1	0	4000	Asymmetry in the upstream magnetic field
C	60	80	0.50	0.25	1	0	2000	Asymmetry in the upstream magnetic field
D	60	80	0.35	0.125	1	0	1000	Asymmetry in the upstream magnetic field
E	60	80	0.50	0.25	1	0	667	Like case C but with triple resistivity
F	60	80	0.50	0.25	1	4	2000	Like case C but with a guide field
G	32	84	0.63	1.0	4	0	5040	Symmetric magnetic field, asymmetric density
H	60	48	0.50	0.25	1	0	8000	Symmetric outflow, periodic in the y-direction

Note. ^a Using Equation (15) assuming $L = 8$.

$$R_0 \equiv \frac{B_{L0}}{B_{R0}} = \frac{1-b}{1+b}, \quad (12)$$

where $0 \leq b < 1$, $B_{L0} > 0$, and $B_{R0} > 0$. These ratios at $t = 0$ will, in general, differ somewhat from the ratios during the course of each simulation.

The initial magnetic perturbation is of the form

$$\mathbf{B}_p = \nabla \times (A_p \hat{\mathbf{z}}), \quad (13)$$

where

$$A_p = -B_p h \exp \left[-\left(\frac{x}{h}\right)^2 - \left(\frac{y-\Delta}{h}\right)^2 \right]. \quad (14)$$

Here, B_p is the strength of the perturbation and h governs the perturbation width. The perturbation is centered about $(x, y) = (0, \Delta)$.

The simulations we report on are presented in Table 1. The controls for our study are case A, with symmetric inflow and asymmetric outflow, and case H, with asymmetric inflow and symmetric outflow. The eight simulations in Table 1 are chosen to test different upstream magnetic field asymmetries (compare cases A–D), different resistivities (cases C and E), the inclusion of a guide field (cases C and F), and different upstream densities (cases A and G). Case C is a control for comparisons with cases E, F, and H which all have $R_0 = 0.25$.

The simulation parameters are as follows. For the initial equilibrium we use $B_0 = 1$, $\delta_0 = 0.1$, and $\beta_{R0} = 0.18$. The initial perturbation is given by $B_p = 0.1$, $\Delta = 1$, and $h = 0.5$, except for case H where $\Delta = 0$. The diffusivities are given by $\eta = \nu = 10^{-3}$, $D = 10^{-4}$, $\chi_{\perp} = 10^{-4}$, and $\chi_{\parallel} = 10^{-2}$. The Lundquist number must be considered carefully because the Alfvén speeds differ in each upstream region. For our comparisons we use a hybrid Lundquist number based on the hybrid Alfvén speed presented in Equation (1),

$$S_h \equiv \frac{LV_{Ah}}{\eta}, \quad (15)$$

where L is the characteristic length scale of the current sheet. Mesh packing is used to concentrate resolution in regions of strong gradients. However, because the current sheets drift in most simulations, high resolution is needed over a larger part of the domain than in simulations with symmetric inflow and/or outflow. We use seventh-order finite element basis functions in all simulations. There are m_x and m_y finite elements along the inflow and outflow directions, respectively. The size of the computational domain for cases A–G is given by

$-7 \leq x \leq 7$ and $0 \leq y \leq 30$. We assume conducting wall outer boundary conditions in all directions for cases A–G; consequently, late in time there is some influence from line-tying along the upper boundary at $y = 30$. However, we concentrate on dynamics far from the unphysical upper boundary ($y \lesssim 18$). Case H differs in that $-15 \leq y \leq 15$ and there are periodic boundary conditions in the y-direction. While we include anisotropic thermal conduction, we neglect radiative losses, coronal heating, and vertical stratification of the atmosphere. The cooling timescale for CME current sheet plasma ($T \sim 5 \times 10^6$ K and $n \sim 5 \times 10^8$ cm⁻³) is about half a day. This is an order of magnitude longer than a dynamical timescale, so we are justified in neglecting radiative losses (see also Imada et al. 2011).

It is appropriate to remark upon our choice of a uniform, explicitly defined resistivity. Occasionally, prior simulations of asymmetric inflow reconnection have used a spatially localized resistivity enhancement (e.g., Borovsky & Hesse 2007). The intended effect is to constrain the position of the X-line. However, this constraint is artificial and likely changes the internal structure of the reconnection region and the scaling behavior. We speculate that this is the reason why the scaling found by Borovsky & Hesse (2007) differs slightly from the analytic prediction made by Cassak & Shay (2007). Some simulations use resistivity as a function of current density or other plasma parameters so that the position of the X-line is not artificially constrained (see, for example, Birn et al. 1996). Alternatively, some simulations of reconnection have used numerical resistivity inherent in the discretization as the sole means of breaking the frozen-in condition, rather than an explicitly defined resistivity or field line breaking mechanism included in the physical model (e.g., Laitinen et al. 2005; Ouellette et al. 2010; Edmondson et al. 2010). Such models are effectively using an ideal MHD algorithm. However, when there is significant numerical reconnection in an ideal MHD simulation, the results are by definition not converged. Therefore, while scaling models for asymmetric reconnection such as those by Cassak & Shay (2007) and Murphy et al. (2010) do not explicitly depend on the dissipation mechanism, the lack of convergence makes ideal MHD simulations poor tests of asymmetric reconnection models. Our choice of a uniform, explicitly defined resistivity avoids artificially constraining the position of the X-line and allows convergence in the numerical simulations.

3. SIMULATION RESULTS

In this section, we describe the principal results of our simulations of line-tied asymmetric reconnection. When making comparisons between the simulations presented in Table 1, it is important to note that the scaling for cases A–D is performed

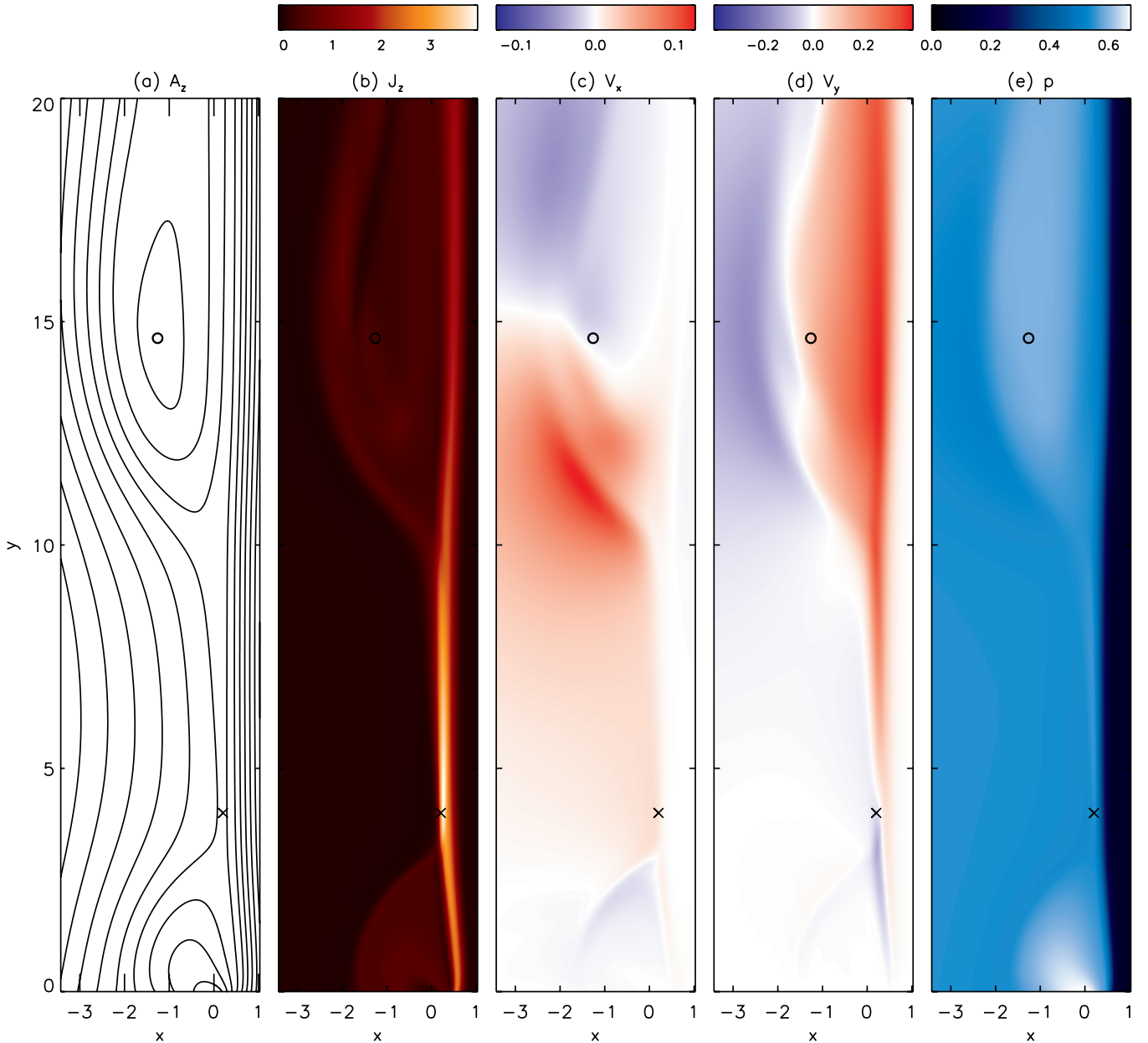


Figure 1. Simulation results for case C with $R_0 = B_{L0}/B_{R0} = 0.25$ at $t = 100$. Shown are (a) the magnetic flux, A_z , (b) the out-of-plane current density, J_z , (c) the inflow component of velocity, V_x , (d) the outflow component of velocity, V_y , and (e) the plasma pressure, p . The “o” denotes the position of the O-point, and the “x” marks the spot of the X-line. Only a portion of the computational domain is shown.

(A color version of this figure is available in the online journal.)

by keeping B_{R0} constant and reducing B_{L0} . Consequently, the total magnetic energy available to be reconnected and the hybrid Alfvén speed given in Equation (1) decrease as the simulations become more asymmetric. Case G is best compared directly to case A, and cases E, F, and H should be compared to case C.

3.1. Principal Features

The general features of our simulations of line-tied asymmetric reconnection are presented in Figure 1, which shows case C with an initial upstream magnetic field ratio of $R_0 = 0.25$. Magnetic flux contours in Figure 1(a) show that field lines in the strong magnetic field region are much less bent than field lines in the weak magnetic field region. The reconnected loops near the lower boundary and the outflow plasmoid both preferentially develop into the weak magnetic field region. The separatrixes

are traced by regions of strong out-of-plane current density in Figure 1(b), but the portions that bound the strong field regions have much stronger current density than the portions that form the boundary between the outflow and weak field regions. The plasma pressure buildup is almost entirely contained on the weak field side of the current sheet (Figure 1(e)).

The upward outflow velocity, shown in Figure 1(d), is substantially faster than the downward outflow velocity because of the obstructing wall along $y = 0$. This behavior is consistent with previous simulations of asymmetric outflow reconnection (Roussev et al. 2001; Galsgaard & Roussev 2002; Oka et al. 2008; Murphy & Sovinec 2008; Murphy 2010; Reeves et al. 2010). This difference in velocities occurs for two principal reasons. First, outflow toward $y = 0$ is obstructed by the buildup of plasma and magnetic pressure. Second, the X-line is located

near the lower exit of the current sheet so that the tension force below the X-line directed toward $y = 0$ is much weaker than the tension force above the X-line directed away from $y = 0$.

In Figure 1(d), there is a stream of plasma flow to the right of the X-line but extending downward into the post-flare loop structure and tracing the separatrix. The magnitude of the plasma flow is small ($V_y \sim 0.02$ compared to $V_{Ah0} = 0.25$), but is positive in a region where negative V_y is expected. Magnetic tension in this region is pulling plasma downward, but is countered by a comparable contribution by the vertical plasma pressure gradient and a modest contribution by the vertical magnetic pressure gradient pushing plasma upward. The current density is strong so that resistive diffusion acts to make the field lines more potential even against this plasma flow. Such flows might be observable, but three-dimensional geometry may make identification ambiguous, and it is not clear that they will occur when $\beta \ll 1$.

3.2. Internal Structure

The X-line (the line about which the magnetic field has a hyperbolic or X-line topology) is located at $\mathbf{x}_n \equiv (x_n, y_n)$. This position is given as a function of time for several simulations in Figure 2. Figure 2(a) shows the X-line position along the inflow direction. In most previous simulations of asymmetric inflow reconnection, the X-line drifts into the region with the stronger magnetic field (e.g., Ugai 2000). This drifting is tied locally to spatial derivatives in the out-of-plane electric field (Murphy 2010). In particular, the X-line drifts along the inflow direction toward decreasing E_z . For many, but not all, of the cases, we observe the X-line drifting toward the strong field upstream region for most of the simulation. In case D with $R_0 = 0.125$, the X-line drifts into the weak field region before drifting into the strong field region. Case E is identical to case C except for having three times the resistivity, and shows a significant drift of the X-line into the weak magnetic field region. Comparing cases A and G suggests that the inclusion of a density asymmetry does not lead to a significant drift along the inflow direction. The rate of X-line drifting along the inflow direction is a function of the magnetic field asymmetry, the resistivity, the inclusion of a guide field, and the simulation setup. However, the dependences on each of these parameters are not straightforward.

The X-line position retreats from the obstruction at $y = 0$ for all asymmetric outflow cases (Figure 2(b)). The rate of X-line retreat is comparable for cases A and B (with $R_0 = 1$ and $R_0 = 0.5$, respectively) but decreases as the initial conditions become more asymmetric. By comparing cases C and E, we see that increasing the resistivity actually slows down X-line retreat, in part because it results in smoother gradients in E_z . From cases A and G, we see that increasing f_0 from one to four decreases the rate of X-line retreat slightly. Comparing cases C and F shows that including a guide field can lead to much faster X-line retreat. In contrast to all other asymmetric outflow simulations, the X-line is located near the top exit of the current sheet in case F.

Previous simulations of reconnection with either asymmetric inflow or asymmetric outflow have generally shown a separation between the flow stagnation point and the principal X-line when a uniform resistivity is used (e.g., Cassak & Shay 2007, 2008, 2009; Oka et al. 2008; Murphy & Sovinec 2008; Murphy 2010; Shen et al. 2011). Contrary to our expectations, there is in general no flow stagnation point associated with the X-line in the simulation reference frame for cases with both asymmetric upstream magnetic fields and asymmetric outflow. There are

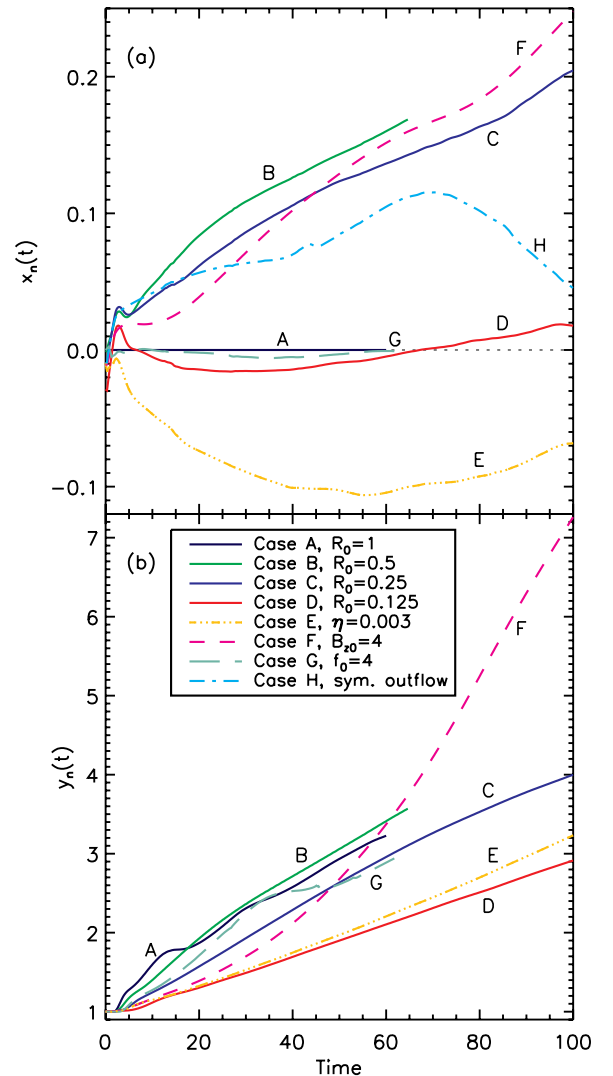


Figure 2. Position of the X-line as a function of time for cases A–H along the (a) inflow and (b) outflow directions. Case H is not shown in the bottom panel because $y_n(t) = 0$ due to symmetry.

(A color version of this figure is available in the online journal.)

contours where $V_x = 0$ and $V_y = 0$, but these contours do not intersect with each other in the current sheet for most of the simulations with asymmetry in both the inflow and outflow directions. There still is a reversal of the outflow component of velocity near but not collocated with the X-line.

Figure 3 shows both the plasma flow velocity at the X-line, $\mathbf{V}_n \equiv (V_x(x_n, y_n), V_y(x_n, y_n))$, and the rate of change in position of the X-line, $\dot{\mathbf{x}}_n \equiv (\dot{x}_n, \dot{y}_n)$, for case C with $R_0 = 0.25$. The plasma flow velocity at the X-line differs greatly from the X-line drift velocity along both the inflow and outflow directions, indicating a significant departure from the frozen-in condition. For the inflow direction, $V_x(x_n, y_n)$ is of the same sign as \dot{x}_n , but $V_x(x_n, y_n)$ is significantly greater. For the outflow direction, \dot{y}_n remains positive but $V_y(x_n, y_n)$ becomes negative so that the X-line is retreating against the flow of the plasma. The X-line is able to diffuse against strong plasma flow by diffusion of B_x along the inflow direction, as described in detail by Murphy (2010; see also Siscoe et al. 2002; Oka et al. 2008).

A slice along the inflow direction for case C at the height of the X-line ($y = y_n$) is given in Figure 4 for $t = 100$. The maximum in J_z is located on the strong field side of the X-line. This result,

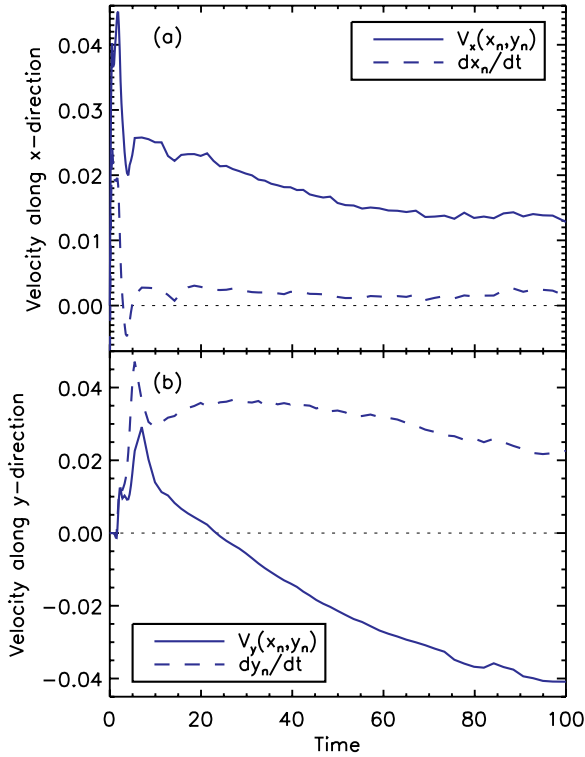


Figure 3. Comparison of the plasma flow velocity at the X-line, $(V_x(x_n, y_n), V_y(x_n, y_n))$, to the time derivative of the position of the X-line, $(dx_n/dt, dy_n/dt)$, for the (a) inflow direction and (b) outflow direction, for case C with $R_0 = 0.25$. The plasma flow velocity at the X-line differs significantly from the rate of X-line motion along both directions.

(A color version of this figure is available in the online journal.)

that the X-line is on the weak field side of the current sheet, is consistent with the simulations of Cassak & Shay (2007). The X-line is located near a local maximum in plasma pressure along the inflow direction. In the simulation reference frame, $V_x \approx 0$ away from the diffusion region on the strong field side of the current sheet. This can be interpreted as most of the inflow coming in from the weak field side, with the X-line and current sheet drifting into the strong field upstream region. The outflow component of velocity, V_y , has an interesting bipolar signature. While the X-line is moving in the positive y -direction, the X-line is located near where V_y is most negative. The inflow component of the magnetic field, B_x , is negative throughout the slice except at the X-line where it is zero. This profile allows negative B_x to diffuse inward so that at later times the X-line is located at higher heights (compare to Figure 5 of Murphy 2010). The reconnecting component of the magnetic field, B_y , shows that the initial ratio of $R_0 = 0.25$ is somewhat less extreme than the ratio of $R \approx 0.17$ at $t = 100$.

3.3. Reconnection Rate

The reconnection rate, defined as the out-of-plane component of the electric field at the X-line, is shown in Figure 5 for each of the cases described in Table 1. Comparing cases A–D shows that decreasing the magnetic asymmetry factor R_0 leads to a corresponding decrease in the reconnection rate. This is qualitatively consistent with the scaling derived by Cassak & Shay (2007). Increasing the density asymmetry factor f_0 decreases the reconnection rate modestly from case A to case G. The reconnection rate in case C is somewhat quicker than case E, even though case E is three times more resistive. The

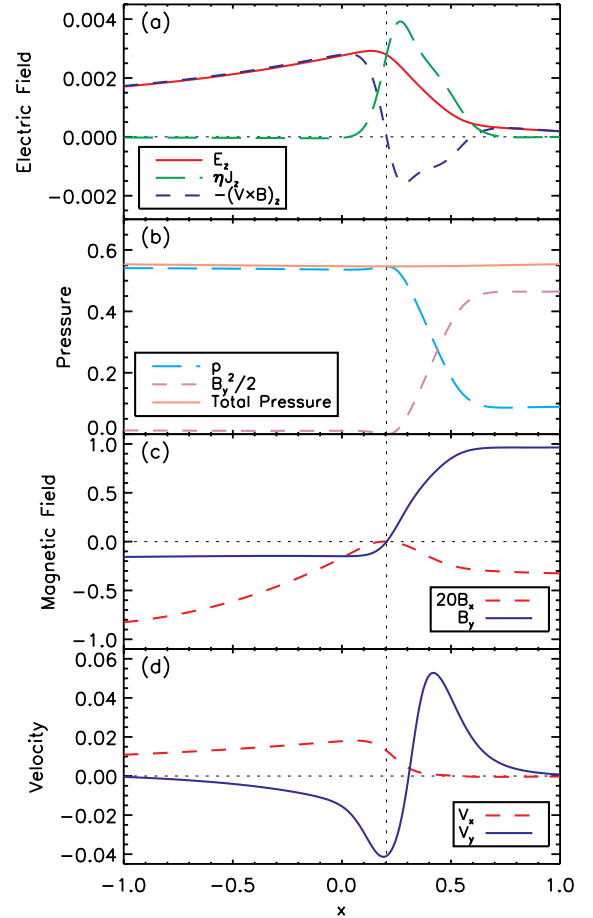


Figure 4. Simulation parameters for a slice along the inflow direction at the position of the X-line for case C with $R_0 = 0.25$ at $t = 100$. The vertical dotted line represents the position of the X-line along the inflow direction. Shown are (a) components of the out-of-plane electric field, (b) contributions to total pressure balance along the inflow direction, (c) components of the in-plane magnetic field, and (d) the inflow and outflow components of velocity.

(A color version of this figure is available in the online journal.)

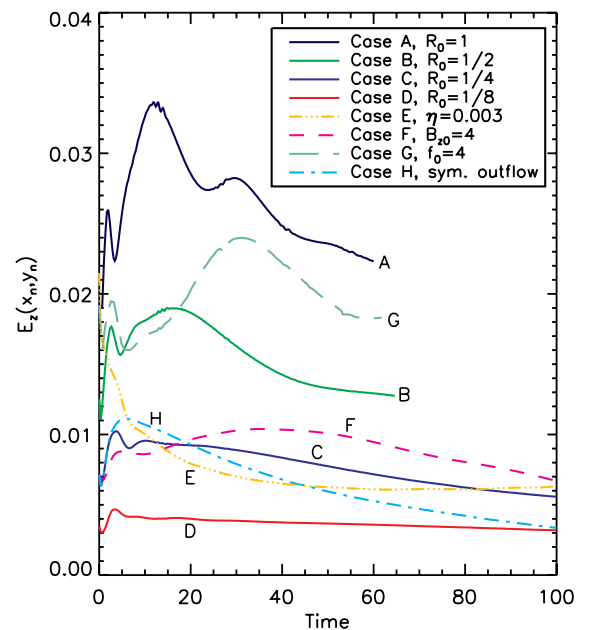


Figure 5. Reconnection electric field strengths at the X-line as a function of time for cases A–H.

(A color version of this figure is available in the online journal.)

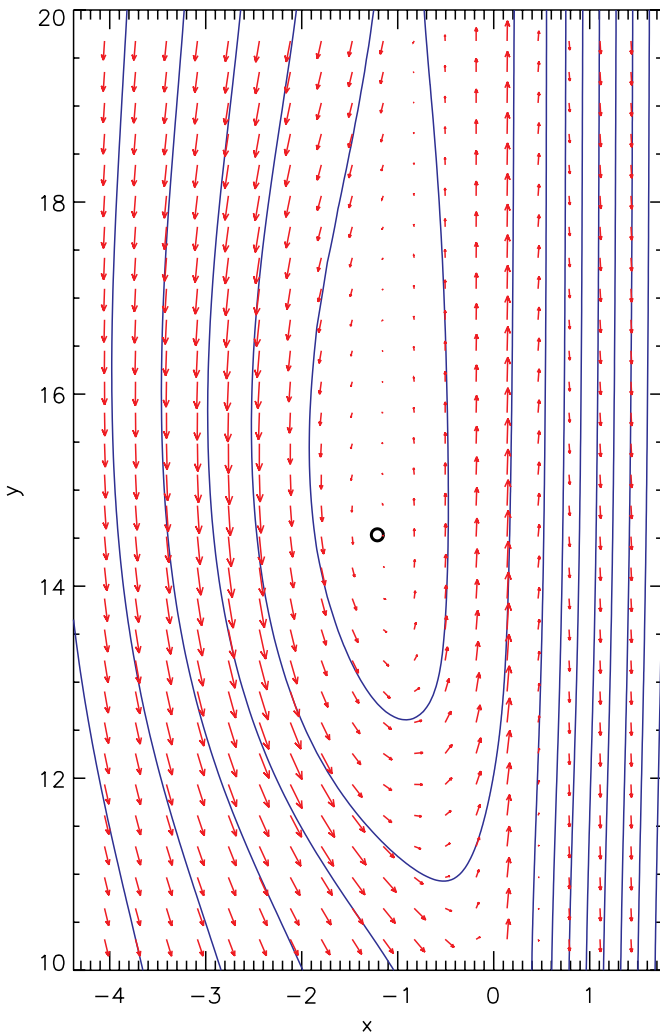


Figure 6. Shown are the magnetic flux (solid blue contours) and flow velocity vectors in the frame of the O-point (red arrows) for case C at $t = 100$. The O-point is denoted by the circle at $(x_o, y_o) = (-1.21, 14.53)$. The flow pattern about the O-point is counterclockwise; consequently, there is net vorticity in the outflow plasmoid.

(A color version of this figure is available in the online journal.)

inclusion of a guide field slightly increases the reconnection rate in case F compared to case C. The reconnection rate is modestly quicker with asymmetric inflow and outflow (case C) than in an otherwise equivalent simulation with asymmetric inflow but symmetric outflow. As described by Murphy (2010), this occurs because the current sheet can only increase in length along one outflow direction.

3.4. The Outflow Plasmoid

The asymmetric inflow condition allows net vorticity in the outflow plasmoid. In Figure 6, we show velocity vectors in the reference frame of the O-point for case C at $t = 100$. The counterclockwise flow pattern is largely due to the reconnection outflow jet impacting the rising plasmoid at an angle; consequently, the outflow jet increases the net vorticity in the plasmoid. This circulation should be a generic feature of asymmetric inflow reconnection but not asymmetric outflow reconnection. This interpretation should be considered qualitatively rather than quantitatively because the presence of closed field lines is partially due to reconnection near the outer, artificial line-tied boundary at $y = 30$. However, these results

suggest that the orientation of reconnection outflow jets relative to the flux rope can lead to an analogous circulation pattern when the outflow jet impacts the flux rope obliquely rather than directly at its base.

In contrast to the X-point, the frozen-in condition near the O-point is approximately met. For example, at $t = 100$ in case C, the plasma flow at the O-point is approximately equal to the velocity of the O-point: $(V_x(x_o, y_o), V_y(x_o, y_o)) = (-0.0076, 0.1211)$ compared to $(\dot{x}_o, \dot{y}_o) = (-0.0065, 0.1238)$, where $\mathbf{x}_o \equiv (x_o, y_o)$ is the position of the O-point. This indicates that the O-point is being primarily advected by the bulk plasma flow and that diffusive flow across the O-point is not significant. Plasma flow across an O-point can occur in a process similar to that described by Murphy (2010) for X-line retreat. When the O-point in a magnetic island is displaced toward one particular direction, resistive diffusion will in general act to change the position of the O-point to be closer to the center of the island when the island is not significantly distorted.

3.5. Morphology of the Post-flare Loops

The most easily observable difference between the symmetric and asymmetric cases is the structure of the post-flare loops. In particular, the asymmetric loops are skewed when compared to the symmetric case, and take an asymmetric candle flame shape. While in the symmetric case the tops of each loop are all along $x = 0$, the loop-tops in the asymmetric case have their apices at different locations along the inflow direction (Figure 7). At low heights where the field has relaxed to a near-potential state, the loop-tops are displaced toward the low magnetic field side. At greater heights, the loop-tops become located closer to the current sheet demarcating the low and high magnetic field regions.

4. AN ANALYTIC SOLUTION FOR THE POTENTIAL FIELD STRUCTURE OF ASYMMETRIC POST-FLARE LOOPS

In Section 3.5 and Figure 7, we show that the location of the post-flare loop apices in each case are a function of height. In the current section, we present an analytic solution for the potential field structure of post-flare loops in the present configuration. This solution provides insight into the observational signatures very near the magnetic field reversal along the lower boundary, but should be treated as a limiting case for post-flare loops late in time that have been able to relax to a near-potential state.

We consider the domain $0 \leq x \leq \pi$ and $y \geq 0$. The boundary condition along $y = 0$ is given by

$$B_y(x, 0) = \begin{cases} -B_L & : 0 < x < a \\ B_R & : a < x < \pi \end{cases}, \quad (16)$$

where the constants B_L and B_R are positive and the location of the field reversal is given by

$$a = \frac{\pi B_R}{B_L + B_R}. \quad (17)$$

Consequently, there is no net magnetic flux from the lower boundary over $0 \leq x \leq \pi$. Because the outer boundary is artificial, we must consider regions close to the magnetic field reversal to avoid these effects. However, this analysis also assumes that the magnetic field reversal length scale is smaller than the region being investigated. Because we are finding a

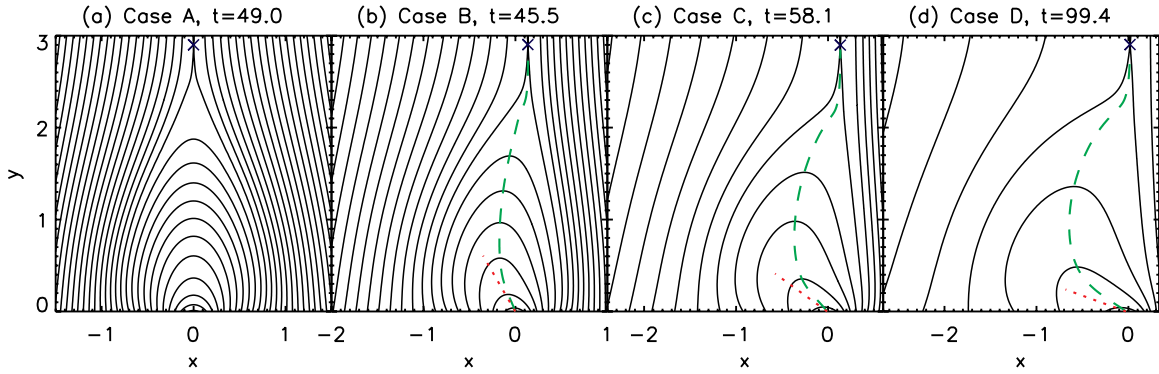


Figure 7. Magnetic flux contours for cases A–D when the X-line in each simulation (denoted by “x”) is located at $y = 2.9$. The dashed green line gives the position of the loop apices (where $B_y = 0$). The red dotted line represents the asymptotic prediction made by Equation (25).

(A color version of this figure is available in the online journal.)

potential field solution, we also require that $\beta \ll 1$, or more generally, that plasma pressure gradient forces are small.

The potential magnetic field is given by

$$\mathbf{B} = -\nabla\psi, \quad (18)$$

where the scalar potential ψ is governed by Laplace’s equation,

$$\nabla^2\psi = 0. \quad (19)$$

The unique solution to Laplace’s equation appropriate to our boundary conditions is

$$\psi = \sum_{n=1}^{\infty} \frac{2}{\pi} \left(\frac{B_L + B_R}{n^2} \right) \sin na \cos nx e^{-ny}. \quad (20)$$

Equation (20) may be written in the form of a vector potential $\mathbf{B} = \nabla \times (A_z \hat{\mathbf{z}})$ to provide an expression for the magnetic flux,

$$A_z = \sum_{n=1}^{\infty} \frac{2}{\pi} \left(\frac{B_L + B_R}{n^2} \right) \sin na \sin nx e^{-ny}. \quad (21)$$

On large scales, the solution depends on the outer boundary. On scales much smaller than the outer boundary, the solution becomes scale-free as we approach $(x, y) \rightarrow (a, 0)$. Because, in general, Fourier series expansions will be truncated at some N_{\max} , we must also consider scales $\Delta x \gg \pi/N_{\max}$. Using Euler’s formula and the identity $\ln(1 - q) = -\sum_{n=1}^{\infty} q^n/n$, the components of the magnetic field are given in closed form by

$$B_x = \frac{B_L + B_R}{2\pi} \ln \left[\frac{(1 - e^{ia+ix-y})(1 - e^{-ia-ix-y})}{(1 - e^{ia-ix-y})(1 - e^{-ia+ix-y})} \right], \quad (22)$$

$$B_y = i \left(\frac{B_L + B_R}{2\pi} \right) \ln \left[\frac{(1 - e^{ia+ix-y})(1 - e^{ia-ix-y})}{(1 - e^{-ia+ix-y})(1 - e^{-ia-ix-y})} \right]. \quad (23)$$

Solutions for four different magnetic field ratios are presented in Figure 8, very close to the magnetic field reversal along the lower boundary. These solutions approximate the magnetic field structure of post-flare loops after these loops have had time to relax. These loops have a similar appearance to the reconnected loops very near the field reversal that are shown in Figure 7.

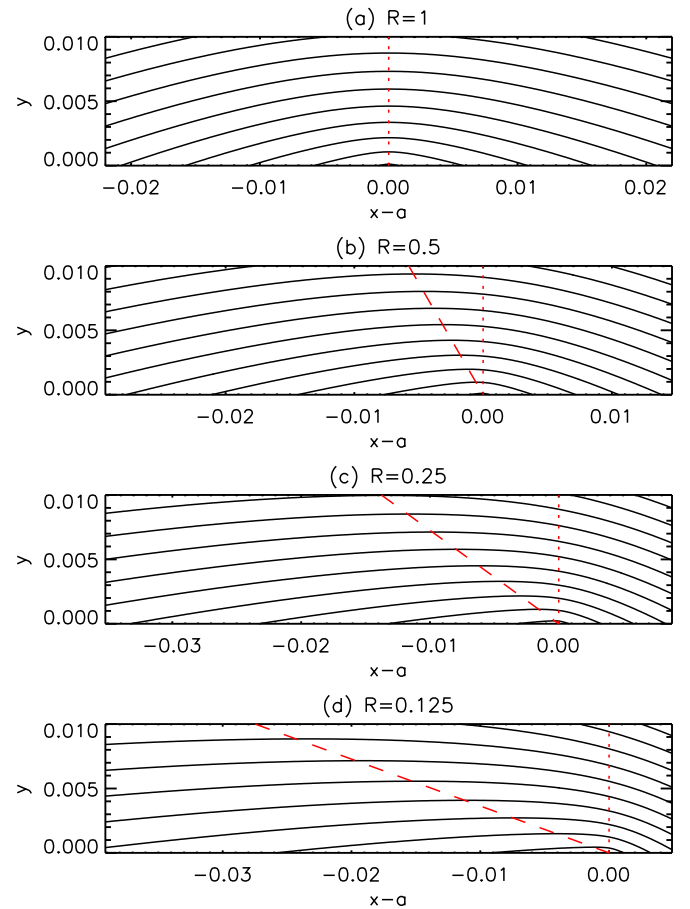


Figure 8. Magnetic flux contours for the analytical potential field solution of asymmetric post-flare loops as given by Equation (21), very near the magnetic field reversal along the lower boundary at $x = a$ (represented by the red dotted vertical line). The dashed red line is the location of the loop-tops as given by Equation (25). The solutions are for magnetic field ratios of (a) $R = 1$, (b) $R = 0.5$, (c) $R = 0.25$, and (d) $R = 0.125$.

(A color version of this figure is available in the online journal.)

Next, we derive the loop-top positions along the inflow direction as a function of height. By setting $B_y = 0$ and using Euler’s formula and trigonometric identities, we can obtain an equation for the height of loop-tops as a function of x . The loop-top positions are given by

$$y_{\text{LT}}(x) = \ln(\cos a \sec x). \quad (24)$$

For our purposes, this expression is most useful near the field reversal along the lower boundary at $(x, y) = (a, 0)$ where the solution is insensitive to the outer boundary. We define $\theta = \arccot(dy_{LT}/dx)$ as the clockwise angle with respect to vertical for the loop-top positions. Because $dy_{LT}/dx = \tan x$ and $R \equiv B_L/B_R$, evaluating Equation (24) at $x = a$ yields

$$\theta = \frac{\pi}{2} \left(\frac{R - 1}{R + 1} \right). \quad (25)$$

Equation (25) provides an upper limit on the distortion of the asymmetric post-flare loops as a function of asymmetry. The angle from vertical for the loop-top positions is shown in both Figures 7 and 8. In Figure 7, we see that Equation (25) reliably approximates the angle from vertical that the loop-top positions take very near the field reversal. Equation (25) overestimates the angle slightly in the simulations because of the finite width of the magnetic reversal along the lower boundary ($\delta_0 = 0.1$) and because the field lines are not fully potential, due in part to a finite pressure gradient.

5. OBSERVATIONAL SIGNATURES OF ASYMMETRIC RECONNECTION

In this section, we describe the observational signatures predicted by our simulations of line-tied asymmetric reconnection during solar eruptions.

5.1. The Location of the X-line and Flow Reversal

The location of the principal X-line is important in flare/CME current sheets because it helps determine the partition of outflow energy toward and away from the Sun. These simulations suggest that, at least during reconnection with a weak guide field, the principal X-line will be located near the lower base of flare/CME current sheets, not too far above the post-flare loops (e.g., Murphy 2010; Shen et al. 2011). The principal X-line and flow reversal are probably separated by a distance that is shorter than the observational errors and systematic uncertainties. Finding the location of the flow reversal in a current sheet viewed nearly edge-on is difficult but can be done by tracking the motions of current sheet blobs. This task has been accomplished by Savage et al. (2010), who find that the flow reversal is at a height of just ~ 0.25 solar radii above the limb in the Cartwheel CME current sheet. For comparison, the post-flare loops have a height between 0.1 and 0.2 solar radii above the limb and the current sheet extends several solar radii outward into the LASCO field of view. Our simulations also predict that the X-line is located on the weak magnetic field side of the current sheet (see Figure 1); however, we anticipate that this signature is beyond our current observational capabilities.

5.2. Post-flare Loops and Loop Footpoints

A signature of line-tied asymmetric reconnection is the distortion or skewing of post-flare loops as shown in Figure 7 and described in Section 3.5. The loop apexes are not immediately above each other. Rather, the apex positions along the inflow direction are a function of height. The post-flare loops develop a characteristic skewed candle flame shape. This signature should be apparent in H α , EUV, and X-ray observations of post-flare loops during line-tied asymmetric reconnection. A candidate event with a clear skewed candle flame shape is the 1992 February 21 flare on the east limb that was analyzed by Tsuneta

et al. (1992) and Tsuneta (1996). However, projection effects associated with a complicated three-dimensional geometry might also lead to a skewed candle flame structure during some events (see, for example, Figure 15 of Forbes & Acton 1996).

Solar flares characteristically show hard X-ray (HXR) emission at the footpoints of newly reconnected field lines in response to energetic particles and the thermal conduction front impacting the chromosphere. The standard model of solar flares predicts that the footpoints move away from the neutral line so that the instantaneous location of the footpoints is given by the amount of reconnected flux (e.g., Lin et al. 1995; Forbes & Acton 1996; Lin 2004). This behavior has been observed during many flares (e.g., Asai et al. 2004; Krucker et al. 2005; Yang et al. 2009, 2011), although more complicated motions are possible (e.g., Bogachev et al. 2005; Sakao et al. 1998; Grigis & Benz 2005; Somov et al. 2005; Ji et al. 2006; Su et al. 2007). Because of the requirement that equal amounts of flux be reconnected from each upstream region in two-dimensional simulations, we predict that the velocity of the footpoint in the strong field region will be slower than the velocity of the footpoint in the weak field region. For example, if the magnetic field in one upstream region has twice the strength of the other region, then the footpoints on the strong magnetic field side will move half as quickly as the footpoints on the weak magnetic field side. By combining observations during the 2003 October 29 X10 flare by the *Reuvan Ramaty High Energy Spectroscopic Imager* and the *Michelson Doppler Interferometer* (Scherrer et al. 1995) on *SOHO*, Krucker et al. (2005) showed that the magnetic field near the slower moving footpoint was generally stronger than in the faster moving footpoint (see also Svestka 1976). While this is consistent with the predictions from our models, theory needs to take into account the three-dimensional nature of magnetic reconnection and the patchy distribution of magnetic flux in the photosphere.

Asymmetry in the post-flare loop structure will affect the relative intensities from the emissions at each footpoint. HXR emission is largely determined by the transport of energetic particles from above the loop-top into the chromosphere. Energetic particles on the strong magnetic field side will be more likely to be reflected because magnetic mirroring is more effective. Therefore, energetic particles will be more likely to enter the lower solar atmosphere on the weak magnetic field side. Consequently, the footpoint on the weak magnetic field side is expected to yield stronger HXR emission and chromospheric evaporation due to beam heating (Melrose & White 1979, 1981; Sakao 1994; Huang 2007). Kundu et al. (1995) present two flares observed by the Nobeyama radioheliograph (Nakajima et al. 1994) and the Hard X-ray Telescope on *Yohkoh* (Kosugi et al. 1991) in support of this scenario. The footpoints with weak HXR emission (indicating fewer particles escaping from the trap) had stronger gyrosynchrotron emission (suggestive of a stronger magnetic field). While this behavior does not happen in all flares (Goff et al. 2004), additional sources of asymmetry include an asymmetric initial pitch angle distribution (e.g., Huang et al. 2010), differences in the column density in each footpoint (see, however, Saint-Hilaire et al. 2008), and directionality in the accelerating electric field (Hamilton et al. 2005; Li & Lin 2012).

5.3. Reconnection Inflow Velocities

Several works have reported observations of reconnection inflow velocities associated with flare/CME current sheets (e.g., Yokoyama et al. 2001; Lin et al. 2005; Narukage & Shibata 2006;

Takasao et al. 2012). During asymmetric inflow reconnection, the inflow velocities on either side of the current sheet are predicted to differ. In a steady-state, one would expect from flux conservation that the out-of-plane electric field will be constant, leading to the relation

$$V_L B_L = V_R B_R. \quad (26)$$

This implies that the ratio of inflow velocities is inversely proportional to the ratio of upstream magnetic field strengths and that, in principle, measuring the ratio of inflow velocities on either side of the current sheet would directly provide the upstream magnetic field ratio.

Figure 4 shows that there are strong variations in the electric field in the simulation reference frame and that the inflow component of velocity is approximately zero in the strong upstream region. Thus, the reconnection process in the simulations is not time-independent. Therefore, Equation (26) should not be expected to give reliable estimates of the magnetic field asymmetry except by taking the velocities in the reference frame of the X-line and showing that the reconnection process is steady. However, despite the inapplicability of Equation (26) during time-dependent asymmetric reconnection, a systematic demonstration that the reconnection inflows differ on either side of the current sheet will provide suggestive evidence in future observations that the reconnection process is asymmetric.

5.4. Drifting of the Current Sheet

A commonly observed feature of CME current sheets is that they appear to drift or tilt with time. *Hinode*/XRT observations of the Cartwheel CME show that the current sheet drifted at a rate of $\sim 4^\circ \text{ hr}^{-1}$ (Savage et al. 2010). Ko et al. (2003) discussed observations on 2002 January 8 of a current sheet with a drift of $\sim 0.8^\circ \text{ hr}^{-1}$. These drift rates are significantly greater than can be accounted for by solar rotation.

There are several possible explanations for the observed drifting of CME current sheets: (1) Savage et al. (2010) suggest that the Cartwheel CME current sheet is observed at an angle to the plane of sky and that the appearance of drifting is caused by different parts of the current sheet actively reconnecting at different times. (2) The tilting could be due to the drifting of the X-line and current sheet into the strong magnetic field region during line-tied asymmetric reconnection as discussed in this paper. The predicted velocity of less than a percent of the Alfvén speed is within observational constraints. However, the simulations show drifting but not the observed tilting of the current sheet. (3) The rising flux rope could pull the plasma sheet region along with it so that the drifting is caused by macroscopic behavior. This mechanism requires that the current sheet become more aligned with the direction of flux rope propagation. For the Cartwheel CME, however, this appears to not be the case. (4) There is a large-scale force imbalance between the two upstream regions so that the entire region surrounding the current sheet is pushed rapidly toward one direction. Such a force imbalance could easily occur in the early stages of an ejection (see Ko et al. 2003). (5) The tilting is caused by relaxation in the post-eruption active region as the magnetic field configuration becomes more potential.

Further numerical and observational tests are required to constrain which mechanisms lead to current sheet drifting during CMEs. The location of the CME current sheet relative to the direction of propagation of the flux rope may be of particular importance in determining how upflow from the current sheet

impacts and influences the evolution of the rising plasmoid. However, it is not yet known if CME current sheets are an important component of the energy and momentum budgets of CMEs.

5.5. Circulation within the Rising Flux Rope

In Section 3.4, we show that the asymmetric inflow condition allows net vorticity to develop in the outflow plasmoid. This circulation pattern develops because the outflow jet impacts the rising flux rope obliquely rather than directly at its base. When the current sheet and direction of flux rope propagation are misaligned, this leads to the possibility that the reconnection outflow jet torques the rising plasmoid. Vortex motions like those seen in Figure 6 are not unique to configurations with a line-tied lower boundary, but rather should be a generic feature of reconnection with asymmetric upstream magnetic fields such as at the dayside magnetopause.

Martin (2003), Panasenco & Martin (2008), and Panasenco et al. (2011) report observations of several CMEs that display a rolling motion about the axis of the erupting prominence. We hypothesize that this rolling motion is induced by an offset between the CME current sheet and the rising flux rope during some events. However, it is unknown if the kinetic energy released by reconnection is enough to drive this circulation.

There are other candidate mechanisms for the development of apparent circulation and vorticity in the rising flux rope when viewed in cross-section. A similar flow pattern could develop by untwisting of the magnetic field in the rising flux rope during expansion and relaxation. Alternatively, the external magnetic field could deflect the flux rope's outward motion, thus leading to apparent rolling behavior. For example, Panasenco et al. (2011) note the presence of coronal holes near CMEs that display rolling motion. This rolling behavior about the flux rope axis is in contrast to rotation about the direction of CME propagation (e.g., Lynch et al. 2009; Patsourakos & Vourlidis 2011; Thompson et al. 2012).

5.6. Ultraviolet Spectroscopy of the Inflow Regions and Current Sheet

If there is a strong asymmetry in the plasma conditions on the two sides of the current sheet, then an asymmetry in the emission line intensities might be expected as well. An example is seen in Figure 12 of Ko et al. (2003), where the [Fe XVIII] and [Ca XIV] lines are sharply peaked at the same position along the slit, while the Si XII emission is shifted about $70''$ (one bin along the entrance slit, or 50 Mm) toward the north, and [Fe XII] is shifted still farther north by another $70''$. Lower temperature lines such as [Fe X] are entirely absent from the immediate area of the current sheet, but a definite [Fe X] feature is seen about $140''$ to the south.

There is a clear asymmetry in the temperature between the north and south sides of the current sheet in Figure 12 of Ko et al. (2003). It is hard to estimate the temperatures accurately because of the ambiguity caused by the uncertainty in the foreground and background contributions to the line intensities. Roughly speaking, the [Fe X] and [Fe XII] intensities on the southern side are comparable, indicating a temperature $\log T \sim 5.95$, while on the northern side Si XII is several times stronger than [Fe XII], suggesting $\log T \sim 6.15$.

The density contrast is more difficult to estimate. Based on those temperatures, the emission measure on the northern side is four times that to the south. Assuming that the depth

along the line of sight is the same on both sides of the current sheet, the density is twice as high to the north. Another density diagnostic is the $\text{Ly}\beta$ to $\text{Ly}\alpha$ ratio. Since $\text{Ly}\beta$ contains comparable contributions from collisionally excited ($\propto n^2$) and radiative scattering ($\propto n$) components, while $\text{Ly}\alpha$ is almost entirely formed by radiative scattering, the ratio is a reliable diagnostic. Unfortunately, the separation of the emission from the region of the current sheet from broad background emission is even more difficult than it is for the Fe and Si lines discussed above. We estimate that the $\text{Ly}\beta$ to $\text{Ly}\alpha$ ratios are 0.01 and 0.006 on the southern and northern sides, respectively, which would imply that the density is ~ 1.5 times higher in the south than in the north. Each of these density diagnostics is accurate to within about a factor of two, suggesting that the northern and southern densities are comparable to within uncertainties. Overall, we conclude that the plasma pressure is somewhat higher in the north than the south. It would be dangerous to conclude that the magnetic pressure is higher in the south than the north, however, since the region is probably not in equilibrium.

Asymmetry in the upstream temperatures might also affect the charge state distribution in the current sheet plasma and the rising flux rope. For example, the two upstream regions could start in ionization equilibrium at $T_L = 1$ and $T_R = 2$ MK. Plasma entering the current sheet will be heated very quickly to ~ 5 – 10 MK. The ionization timescales typically range from 10 to 1000 s and are a function of both temperature and density. This is comparable to a dynamical timescale, and thus we expect the plasma leaving the current sheet to be underionized (Ko et al. 2010; Imada et al. 2011). Because the current sheet plasma contains contributions from upstream plasma with different initial temperatures, this may result in a broader charge state distribution than would be expected if there was just one starting temperature. However, the difference may be small because the timescales to ionize low charge state species will be short in very hot plasma. Differences in the inflow velocities, densities, and temperatures might also lead to observable differences in the non-thermal line widths between the two upstream regions.

6. DISCUSSION AND CONCLUSIONS

In this article, we present resistive MHD simulations of line-tied asymmetric reconnection in the context of solar flare and CME current sheets. There is asymmetry along the inflow direction because of different upstream densities and magnetic field strengths, and asymmetry along the outflow direction because the initial perturbation is placed near a conducting wall. The simulations are used to understand the basic physics of asymmetric reconnection and predict observational signatures of asymmetric reconnection in the solar atmosphere. This approach provides a unified picture of how asymmetry in the reconnection process impacts flare emissions and CME evolution.

As in previous simulations of asymmetric outflow reconnection, the X-line is generally located near the lower base of the current sheet. Consequently, the outflow velocity in the unobstructed direction is significantly faster than the outflow velocity in the obstructed direction. The slow downflows occur in simulations for two reasons. First, the downflows impact a region of strong magnetic and plasma pressure, thus slowing them down. Second, the principal X-line is often located near the lower base of the current sheet so that the downward tension force is much weaker compared to the upward tension force. Downflowing loops in flare/CME current sheets are frequently observed to propagate at velocities several times slower than the Alfvén

speed (McKenzie & Hudson 1999; Asai et al. 2004; Sheeley et al. 2004; Reeves et al. 2008; Savage & McKenzie 2011; Warren et al. 2011; McKenzie 2011), in contrast to symmetric models of reconnection that predict bidirectional Alfvénic jets. Simulations such as those presented in this paper suggest that the outflow asymmetry is responsible for this difference in outflow speeds (see also Roussev et al. 2001; Galsgaard & Roussev 2002; Reeves et al. 2010; Murphy 2010; Shen et al. 2011). Observational analysis techniques such as those by Savage et al. (2010) that constrain the position of the reconnection flow reversal are important for resolving the problem of slow downflows. We do note that there are observations of fast downflows during some reconnection events (e.g., Innes et al. 2003).

In simulations with asymmetric upstream magnetic fields, we find that the post-flare loops are skewed when compared to cases with symmetric inflow. The loop-tops are not directly above each other; rather, the positions of the loop-tops are a function of height. The observed shape of these loops is reminiscent of a candle flame. The structure of near-potential loops close to the field reversal along the lower boundary are approximately given by our analytic solution in Section 4. Cuspy post-flare loops with an apparent candle flame structure have been observed during many events (Tsuneta et al. 1992; Tsuneta 1996; Forbes & Acton 1996; Reeves et al. 2008). Observations showing such behavior would allow us to diagnose or place limits on the asymmetry in the upstream magnetic fields. However, three-dimensional geometry and projection effects would need to be considered carefully because they could also contribute to a skewed post-flare loop appearance (see Forbes & Acton 1996).

The morphological features associated with line-tied asymmetric reconnection grow preferentially into the weak magnetic field upstream region. Unlike in cases with symmetric inflow, there is net vorticity in the outflow plasmoid because the reconnection outflow jet impacts it obliquely. This result suggests that CME current sheets could drive a circulation pattern in erupting flux ropes when viewed in cross-section for events where the current sheet is offset from the direction of flux rope motion.

The X-line retreats away from the obstructing wall in all simulations where it is present (see also Oka et al. 2008; Murphy 2010), while generally staying near the lower base of the current sheet. The exception is case F with a strong guide field, which shows that the X-line becomes located near the top exit of the current sheet. The X-line drifts toward the upstream region with the stronger magnetic field in most simulations with asymmetric inflow (e.g., Ugai 2000; Cassak & Shay 2007). During simulations with symmetric upstream magnetic fields but asymmetric upstream densities, the X-line does not drift significantly along the inflow direction.

For each simulation, we find that the plasma flow velocity at the X-line is substantially different from the time derivative of the X-line's position. Any difference between these two velocities must be due to resistive diffusion (e.g., Seaton 2008; Murphy 2010). With the exception of the guide field and symmetric outflow cases, the X-line retreats along the outflow direction against the flow of the plasma. This occurs because diffusion of the inflow component of the magnetic field along the inflow direction is able to shift the X-line position (Murphy 2010). During reconnection with asymmetric inflow, the inflow component of plasma velocity at the X-line is in the same direction as the time derivative of the X-line position along the inflow direction. However, the plasma flow velocity is much faster than the rate of change in position of the X-line along the inflow direction. Consequently, one must be careful when

converting simulations to the reference frame of the X-line because the plasma flow velocity will likely be different.

While our simulations provide significant insight into the basic physics and observational consequences of line-tied asymmetric reconnection in the solar atmosphere, it is important to note the limitations of our models. Most noticeably, β is larger in the simulations than in most of the corona. Because the simulations start from a perturbed initial equilibrium, total pressure balance is enforced along the inflow direction by increasing plasma pressure on the weak magnetic field side. It is difficult to maintain a large asymmetry in low- β plasmas. The asymmetries in the simulations are probably more extreme than in the solar atmosphere. We speculate that magnetic field asymmetries of $\sim 10\%$ – 25% are common, with differences of perhaps $\gtrsim 50\%$ possible in more extreme cases. The assumption of an initial equilibrium is also questionable since CMEs are non-equilibrium events. The simulations do not include radiative cooling, coronal heating (except for viscous and Ohmic heating), or initial vertical stratification of the solar atmosphere. The outer conducting wall boundary conditions will affect the results on long timescales by additional line-tying as well as pileup of reconnection exhaust. The Lundquist numbers in our simulations are $\lesssim 10^4$, so our current sheets are below the $S \sim 5 \times 10^4$ threshold for the onset of the plasmoid instability (e.g., Loureiro et al. 2007; Bhattacharjee et al. 2009; Huang & Bhattacharjee 2010; Shepherd & Cassak 2010; Bárta et al. 2008, 2011; Ni et al. 2010; Shen et al. 2011; Biskamp 1986). Our simulations consequently have only one X-line.

Future work on this problem should be performed using a combination of observations and improved numerical simulations. In particular, more realistic initial configurations will provide more detailed predictions that can be compared directly to observations. The HyLoop suite of codes (Winter 2009; Winter et al. 2011) has the ability to take asymmetric loop configurations directly from these simulations, inject a population of energetic particles, and predict flare emissions in detail. Observationally, investigations of candle flame post-flare loops, current sheet drifting, and footpoint motion and relative intensities will provide constraints on the theoretical models. In particular, events that display multiple signatures will provide the most useful constraints and provide the most complete story.

Many open questions remain for asymmetric reconnection in the solar atmosphere. They include: (1) How asymmetric are typical flare/CME current sheets? (2) What mechanisms are responsible for asymmetric HXR footpoint emission during flares? (3) What causes the drifting motion observed in many flare/CME current sheets? (4) Where is the principal X-line in these current sheets? (5) How important are CME current sheets to the eruption as a whole? (6) Are CME current sheets able to instigate circulation in the rising flux rope? (7) What are the effects of the patchy distribution of magnetic flux in the photosphere? We hope to address these problems in future work.

The authors thank P. A. Cassak, S. E. Guidoni, Y.-K. Ko, D. E. McKenzie, L. Ni, M. Oka, S. L. Savage, C. Shen, C. R. Sovinec, H. P. Warren, D. Webb, Y.-H. Yang, and S. Zenitani for useful discussions. This research is supported by NASA grants NNX09AB17G and NNX11AB61G and NASA contract NNM07AB07C to the Smithsonian Astrophysical Observatory. M.P.M. acknowledges support from NASA grant NNX09AH22G. C.L.P. acknowledges support from the NSF-REU solar physics program at the Center for Astrophysics, grant number ATM-0851866. K.K.R. is supported under the

NSF-SHINE program, grant number ATM0752257. The work of J.L. was also supported by the Program 973 grant 2011CB811403, the NSFC grant 10873030, and the CAS grant KJCX2-EW-T07 to the Yunnan Astronomical Observatory. D.B.S. acknowledges support from the Belgian Federal Science Policy Office through ESA-PRODEX grant number 4000103240. N.A.M. acknowledges the hospitality of the Yunnan Astronomical Observatory during a visit supported by CAS grant 2010Y2JB16. The authors thank members of the NIMROD team for code development efforts that helped make this work possible. Resources supporting this work were provided by the NASA High-End Computing (HEC) Program through the NASA Advanced Supercomputing (NAS) Division at Ames Research Center. This article has benefited greatly from the use of NASA's Astrophysics Data System.

REFERENCES

- Al-Hachami, A. K., & Pontin, D. I. 2010, *A&A*, 512, A84
- Asai, A., Yokoyama, T., Shimojo, M., & Shibata, K. 2004, *ApJ*, 605, L77
- Bárta, M., Büchner, J., Karlický, M., & Skála, J. 2011, *ApJ*, 737, 24
- Bárta, M., Vršnak, B., & Karlický, M. 2008, *A&A*, 477, 649
- Beidler, M. T., & Cassak, P. A. 2011, *Phys. Rev. Lett.*, 107, 255002
- Bemporad, A. 2008, *ApJ*, 689, 572
- Bemporad, A., Poletto, G., Suess, S. T., et al. 2006, *ApJ*, 638, 1110
- Bhattacharjee, A., Huang, Y.-M., Yang, H., & Rogers, B. 2009, *Phys. Plasmas*, 16, 112102
- Birn, J., Borovsky, J. E., & Hesse, M. 2008, *Phys. Plasmas*, 15, 032101
- Birn, J., Borovsky, J. E., Hesse, M., & Schindler, K. 2010, *Phys. Plasmas*, 17, 052108
- Birn, J., Hesse, M., & Schindler, K. 1996, *J. Geophys. Res.*, 101, 12939
- Biskamp, D. 1986, *Phys. Fluids*, 29, 1520
- Bogachev, S. A., Somov, B. V., Kosugi, T., & Sakao, T. 2005, *ApJ*, 630, 561
- Borovsky, J. E., & Hesse, M. 2007, *Phys. Plasmas*, 14, 102309
- Brueckner, G. E., Howard, R. A., Koomen, M. J., et al. 1995, *Sol. Phys.*, 162, 357
- Cassak, P. A., & Shay, M. A. 2007, *Phys. Plasmas*, 14, 102114
- Cassak, P. A., & Shay, M. A. 2008, *Geophys. Res. Lett.*, 35, L19102
- Cassak, P. A., & Shay, M. A. 2009, *Phys. Plasmas*, 16, 055704
- Ciaravella, A., & Raymond, J. C. 2008, *ApJ*, 686, 1372
- Ciaravella, A., Raymond, J. C., Li, J., et al. 2002, *ApJ*, 575, 1116
- Edmondson, J. K., Antiochos, S. K., DeVore, C. R., & Zurbuchen, T. H. 2010, *ApJ*, 718, 72
- Fermo, R. L., Drake, J. F., & Swisdak, M. 2010, *Phys. Plasmas*, 17, 010702
- Forbes, T. G., & Acton, L. W. 1996, *ApJ*, 459, 330
- Galsgaard, K., & Pontin, D. I. 2011, *A&A*, 534, A2
- Galsgaard, K., & Rouseff, I. 2002, *A&A*, 383, 685
- Goff, C. P., Matthews, S. A., van Driel-Gesztelyi, L., & Harra, L. K. 2004, *A&A*, 423, 363
- Gray, T., Lukin, V. S., Brown, M. R., & Cothran, C. D. 2010, *Phys. Plasmas*, 17, 102106
- Grigis, P. C., & Benz, A. O. 2005, *ApJ*, 625, L143
- Hamilton, B., Fletcher, L., McClements, K. G., & Thyagaraja, A. 2005, *ApJ*, 625, 496
- Hirayama, T. 1974, *Sol. Phys.*, 34, 323
- Huang, G., Song, Q., & Huang, Y. 2010, *ApJ*, 723, 1806
- Huang, G.-L. 2007, *New Astron.*, 12, 483
- Huang, Y.-M., & Bhattacharjee, A. 2010, *Phys. Plasmas*, 17, 062104
- Imada, S., Murakami, I., Watanabe, T., Hara, H., & Shimizu, T. 2011, *ApJ*, 742, 70
- Innes, D. E., McKenzie, D. E., & Wang, T. 2003, *Sol. Phys.*, 217, 267
- Inomoto, M., Gerhardt, S. P., Yamada, M., et al. 2006, *Phys. Rev. Lett.*, 97, 135002
- Ji, H., Huang, G., Wang, H., et al. 2006, *ApJ*, 636, L173
- Ko, Y.-K., Raymond, J. C., Lin, J., et al. 2003, *ApJ*, 594, 1068
- Ko, Y.-K., Raymond, J. C., Vršnak, B., & Vujčić, E. 2010, *ApJ*, 722, 625
- Kohl, J. L., Esser, R., Gardner, L. D., et al. 1995, *Sol. Phys.*, 162, 313
- Kopp, R. A., & Pneuman, G. W. 1976, *Sol. Phys.*, 50, 85
- Kosugi, T., Makishima, K., Murakami, T., et al. 1991, *Sol. Phys.*, 136, 17
- Krucker, S., Fivian, M. D., & Lin, R. P. 2005, *Adv. Space Res.*, 35, 1707
- Ku, H. C., & Sibeck, D. G. 1997, *J. Geophys. Res.*, 102, 2243
- Kundu, M. R., Nitta, N., White, S. M., et al. 1995, *ApJ*, 454, 522

- Laitinen, T. V., Pulkkinen, T. I., Palmroth, M., Janhunen, P., & Koskinen, H. E. J. 2005, *Ann. Geophys.*, **23**, 3753
- Landi, E., Raymond, J. C., Miralles, M. P., & Hara, H. 2010, *ApJ*, **711**, 75
- Landi, E., Raymond, J. C., Miralles, M. P., & Hara, H. 2012, *ApJ*, in press
- Li, Y., & Lin, J. 2012, *Sol. Phys.*, **277**, 1
- Lin, J. 2004, *Sol. Phys.*, **222**, 115
- Lin, J., & Forbes, T. G. 2000, *J. Geophys. Res.*, **105**, 2375
- Lin, J., Forbes, T. G., Priest, E. R., & Bungey, T. N. 1995, *Sol. Phys.*, **159**, 275
- Lin, J., Ko, Y.-K., Sui, L., et al. 2005, *ApJ*, **622**, 1251
- Lin, J., Li, J., Ko, Y.-K., & Raymond, J. C. 2009, *ApJ*, **693**, 1666
- Lin, J., Raymond, J. C., & van Ballegooijen, A. A. 2004, *ApJ*, **602**, 422
- Lin, Y., Wang, X. Y., Brown, M. R., Schaffer, M. J., & Cothran, C. D. 2008, *Plasma Phys. Control. Fusion*, **50**, 074012
- Linton, M. G. 2006, *J. Geophys. Res.*, **111**, A12S09
- Liu, R., Lee, J., Wang, T., et al. 2010, *ApJ*, **723**, L28
- Loureiro, N. F., Samtaney, R., Schekochihin, A. A., & Uzdensky, D. A. 2011, *Phys. Plasmas*, **19**, 042303
- Loureiro, N. F., Schekochihin, A. A., & Cowley, S. C. 2007, *Phys. Plasmas*, **14**, 100703
- Lukin, V. S., & Linton, M. G. 2011, *Nonlinear Process. Geophys.*, **18**, 871
- Lynch, B. J., Antiochos, S. K., Li, Y., Luhmann, J. G., & DeVore, C. R. 2009, *ApJ*, **697**, 1918
- Martin, S. F. 2003, *Adv. Space Res.*, **32**, 1883
- McKenzie, D. E. 2011, *Phys. Plasmas*, **18**, 111205
- McKenzie, D. E., & Hudson, H. S. 1999, *ApJ*, **519**, L93
- Melrose, D. B., & White, S. M. 1979, *Proc. Astron. Soc. Aust.*, **3**, 369
- Melrose, D. B., & White, S. M. 1981, *J. Geophys. Res.*, **86**, 2183
- Murphy, N. A. 2010, *Phys. Plasmas*, **17**, 112310
- Murphy, N. A., Raymond, J. C., & Korreck, K. E. 2011, *ApJ*, **735**, 17
- Murphy, N. A., & Sovinec, C. R. 2008, *Phys. Plasmas*, **15**, 042313
- Murphy, N. A., Sovinec, C. R., & Cassak, P. A. 2010, *J. Geophys. Res.*, **115**, A09206
- Nakajima, H., Nishio, M., Enome, S., et al. 1994, *Proc. IEEE*, **82**, 705
- Narukage, N., & Shibata, K. 2006, *ApJ*, **637**, 1122
- Ni, L., Germaschewski, K., Huang, Y.-M., et al. 2010, *Phys. Plasmas*, **17**, 052109
- Øieroset, M., Phan, T. D., & Fujimoto, M. 2004, *Geophys. Res. Lett.*, **31**, L12801
- Oka, M., Fujimoto, M., Nakamura, T. K. M., Shinohara, I., & Nishikawa, K.-I. 2008, *Phys. Rev. Lett.*, **101**, 205004
- Oka, M., Phan, T.-D., Eastwood, J. P., et al. 2011, *Geophys. Res. Lett.*, **382**, 20105
- Ono, Y., Inomoto, M., Okazaki, T., & Ueda, Y. 1997, *Phys. Plasmas*, **4**, 1953
- Ono, Y., Morita, A., Katsurai, M., & Yamada, M. 1993, *Phys. Fluids B*, **5**, 3691
- Ouellette, J. E., Rogers, B. N., Wiltberger, M., & Lyon, J. G. 2010, *J. Geophys. Res.*, **115**, A08222
- Panasenco, O., & Martin, S. F. 2008, in *ASP Conf. Ser.* 383, *Subsurface and Atmospheric Influences on Solar Activity*, ed. R. Howe, R. W. Komm, K. S. Balasubramaniam, & G. J. D. Petrie (San Francisco, CA: ASP), 243
- Panasenco, O., Martin, S., Joshi, A. D., & Srivastava, N. 2011, *J. Atmos. Sol.-Terr. Phys.*, **73**, 1129
- Patsourakos, S., & Vourlidis, A. 2011, *A&A*, **525**, A27
- Phan, T. D., Gosling, J. T., Paschmann, G., et al. 2010, *ApJ*, **719**, L199
- Phan, T. D., & Paschmann, G. 1996, *J. Geophys. Res.*, **101**, 7801
- Rakowski, C. E., Laming, J. M., & Lepri, S. T. 2007, *ApJ*, **667**, 602
- Reeves, K. K., & Golub, L. 2011, *ApJ*, **727**, L52
- Reeves, K. K., Linker, J. A., Mikić, Z., & Forbes, T. G. 2010, *ApJ*, **721**, 1547
- Reeves, K. K., Seaton, D. B., & Forbes, T. G. 2008, *ApJ*, **675**, 868
- Rogers, B., & Zakharov, L. 1995, *Phys. Plasmas*, **2**, 3420
- Roussev, I., Galsgaard, K., Erdélyi, R., & Doyle, J. G. 2001, *A&A*, **370**, 298
- Saint-Hilaire, P., Krucker, S., & Lin, R. P. 2008, *Sol. Phys.*, **250**, 53
- Saint-Hilaire, P., Krucker, S., & Lin, R. P. 2009, *ApJ*, **699**, 245
- Sakao, T. 1994, PhD thesis, Univ. Tokyo
- Sakao, T., Kosugi, T., & Masuda, S. 1998, in *Observational Plasma Astrophysics: Five Years of YOHKO and Beyond*, ed. T. Watanabe, T. Kosugi, & A. C. Sterling (Astrophysics and Space Science Library, Vol. 229; Boston, MA: Kluwer), 273
- Savage, S. L., Holman, G., Reeves, K. K., et al. 2011, arXiv:1111.1945
- Savage, S. L., & McKenzie, D. E. 2011, *ApJ*, **730**, 98
- Savage, S. L., McKenzie, D. E., Reeves, K. K., Forbes, T. G., & Longcope, D. W. 2010, *ApJ*, **722**, 329
- Scherer, P. H., Bogart, R. S., Bush, R. I., et al. 1995, *Sol. Phys.*, **162**, 129
- Schettino, G., Poletto, G., & Romoli, M. 2010, *ApJ*, **708**, 1135
- Seaton, D. B. 2008, PhD thesis, Univ. New Hampshire
- Servidio, S., Matthaeus, W. H., Shay, M. A., Cassak, P. A., & Dmitruk, P. 2009, *Phys. Rev. Lett.*, **102**, 115003
- Servidio, S., Matthaeus, W. H., Shay, M. A., et al. 2010, *Phys. Plasmas*, **17**, 032315
- Sheeley, N. R., Jr., Warren, H. P., & Wang, Y.-M. 2004, *ApJ*, **616**, 1224
- Shen, C., Lin, J., & Murphy, N. A. 2011, *ApJ*, **737**, 14
- Shepherd, L. S., & Cassak, P. A. 2010, *Phys. Rev. Lett.*, **105**, 015004
- Siscoe, G. L., Erickson, G. M., Sonnerup, B. U. Ö., et al. 2002, *Geophys. Res. Lett.*, **29**, 1626
- Somov, B. V., Kosugi, T., Bogachev, S. A., Sakao, T., & Masuda, S. 2005, *Adv. Space Res.*, **35**, 1700
- Sovinec, C. R., Glasser, A. H., Gianakon, T. A., et al. 2004, *J. Comput. Phys.*, **195**, 355
- Sovinec, C. R., King, J. R., & NIMROD Team, 2010, *J. Comput. Phys.*, **229**, 5803
- Sovinec, C. R., Schnack, D. D., Pankin, A. Y., et al. 2005, *J. Phys. Conf. Ser.*, **16**, 25
- Sturrock, P. A. 1966, *Nature*, **211**, 695
- Su, Y., Golub, L., & Van Ballegooijen, A. A. 2007, *ApJ*, **655**, 606
- Sui, L., & Holman, G. D. 2003, *ApJ*, **596**, L251
- Svestka, Z. 1976, *Solar Flares* (Dordrecht: Reidel)
- Swisdak, M., Rogers, B. N., Drake, J. F., & Shay, M. A. 2003, *J. Geophys. Res.*, **108**, 1218
- Takasao, S., Asai, A., Isobe, H., & Shibata, K. 2012, *ApJ*, **745**, L6
- Thompson, W. T., Kliem, B., & Török, T. 2012, *Sol. Phys.*, **276**, 241
- Tsuneta, S. 1996, *ApJ*, **456**, 840
- Tsuneta, S., Hara, H., Shimizu, T., et al. 1992, *PASJ*, **44**, L63
- Ugai, M. 2000, *Phys. Plasmas*, **7**, 867
- Uzdensky, D. A., Loureiro, N. F., & Schekochihin, A. A. 2010, *Phys. Rev. Lett.*, **105**, 235002
- Vršnak, B., Poletto, G., Vujčić, E., et al. 2009, *A&A*, **499**, 905
- Warren, H. P., O'Brien, C. M., & Sheeley, N. R., Jr. 2011, *ApJ*, **742**, 92
- Webb, D. F., Burkepile, J., Forbes, T. G., & Riley, P. 2003, *J. Geophys. Res.*, **108**, 1440
- Winter, H. D., III 2009, PhD thesis, Montana State Univ.
- Winter, H. D., Martens, P., & Reeves, K. K. 2011, *ApJ*, **735**, 103
- Yamada, M., Ji, H., Hantao, H., Scott, et al. 1997, *Phys. Plasmas*, **4**, 1936
- Yang, Y.-H., Cheng, C. Z., Krucker, S., & Hsieh, M.-S. 2011, *ApJ*, **732**, 15
- Yang, Y.-H., Cheng, C. Z., Krucker, S., Lin, R. P., & Ip, W. H. 2009, *ApJ*, **693**, 132
- Yokoyama, T., Akita, K., Morimoto, T., Inoue, K., & Newmark, J. 2001, *ApJ*, **546**, L69